Journal of Physics and Chemistry of Solids 74 (2013) 1538–1545

Contents lists available at SciVerse ScienceDirect

Journal of Physics and Chemistry of Solids

journal homepage: www.elsevier.com/locate/jpcs

Synthesis and characterization of silver/lithium cobalt oxide ($Ag/LiCoO_2$) nanofibers via sol–gel electrospinning

Yakup Aykut [a,c,d,*], Behnam Pourdeyhimi [a,b,c], Saad A. Khan [b,c,**]

[a] Fiber and Polymer Science, Department of Textile Engineering, Chemistry and Science, North Carolina State University, Raleigh, NC 27695-8301, USA
[b] Department of Chemical and Biomolecular Engineering, North Carolina State University, Raleigh, NC 27695-7905, USA
[c] Nonwovens Cooperative Research Center, North Carolina State University, Raleigh, NC 27695-803, USA
[d] Department of Textile Engineering, Uludag University, Gorukle, Bursa 16059, Turkey

ARTICLE INFO

Article history:
Received 22 October 2012
Received in revised form
13 May 2013
Accepted 21 May 2013
Available online 4 June 2013

Keywords:
Nanostructures
Sol-gel growth
Crystal structure
Microstructure

ABSTRACT

We report on the preparation and characterization of $Ag/LiCoO_2$ nanofibers (NFs) via the sol–gel electrospinning (ES) technique. Ag nanoparticles (NPs) were produced in an aqueous polyvinyl pyrrolidone (PVP) solution by using $AgNO_3$ precursor. A viscous lithium acetate/cobalt acetate/polyvinylalcohol/water ($LiAc/(CoAc)_2$/PVA/water) solution was prepared separately. A Ag NPs/PVP/water solution was prepared and added to this viscous solution and magnetically stirred to obtain the final homogeneous electrospinning solution. After establishing the proper electrospinning conditions, as-spun precursor $Ag/LiAc/Co(Ac)_2$/PVA/PVP NFs were formed and calcined in air at a temperature of 600 °C for 3 h to form well-crystallized porous $Ag/LiCoO_2$ NFs. Various analytical characterization techniques such as UV–vis, SEM, TEM, TGA, XRD, and XPS were performed to analyze Ag NPs, as-spun and calcined NFs. It was established that Ag NPs in the precursor $Ag/LiAc/Co(Ac)_2$/PVA/PVP NFs are highly self-aligned as a result of the behavior of Ag in the electric field of the electrospinning setup and the interaction of Ag ions with Li and Co ions in the NF. $Ag/LiCoO_2$ NFs exhibit a nanoporous structure compared with undoped $LiCoO_2$ NFs because the atomic radius of Ag is larger than the radius of Co and Li ion; thus, no substitution between Ag and Li or Ag and Co atoms occurs, and Ag NPs are located at the interlayer of $LiCoO_2$ while some are left in the fiber.

1. Introduction

Lithium-transition metals and some of their oxides, such as $LiCoO_2$, LiV_2O_5, $Li_4Ti_5O_{12}$, $LiMn_2O_2$, $LiCuO_2$, LiMnCrO, $LiFePO_4$, and $LiNiO_2$ have been used as cathode materials in high performance lithium-ion rechargeable batteries [1–6]. Among these, all cathode materials, $LiCoO_2$ has potential to be used as a lithium-ion battery cathode because of its layered crystalline structure, good capacity, high cell voltage, high specific energy density, high power rate, low self-discharge and excellent cycle life [6–10]. $LiCoO_2$ has been produced in the form of powders, fibers, and films by using various processing techniques including the sol–gel procedure, precipitation, hydrothermal, metallo-organic decomposition, radio frequency magnetron sputtering, pulsed laser deposition, and soft mechanochemically assisted synthesis [6,9–15].

The electrochemical performance of $LiCoO_2$ can be increased with doping some substituting elements such as Mn, Cr, Ni, Ti, and B [16–20]. According to Alcantara et al. [16], boron-doped $LiCoO_2$ exhibits a higher capacity of the first discharge, enhancement in capacity retention, and improvement in the reversibility of the lithium deintercalation–intercalation process. Waki et al. claimed an improvement in the kinetic reversibility and the cycle stability of $LiCoO_2$ with Mn-substitution by Co atoms [17]. In a recent publication by Stoyanova et al. [18], an improvement in the reversibility and discharge capacity was reported with Mn-substitution. Mladenov et al. claimed the enhanced reversible cycling behavior of $LiCoO_2$ with Mg doping in Li-ion batteries because of the substitution of Co by Mg [19]. Substitution of Co by Cr in $LiCoO_2$ and its effect as a cathode material, examined by Mladenov et al. [20], demonstrated a poor reversible cycling that is of limited use in Li-ion batteries. Titanium-doped $LiCoO_2$ has also been examined and its electrochemical performance in Li-ion batteries was reported by Gopukumar et al., where enhanced stable electrochemical capacity was demonstrated [21].

On the other hand, doping with a non-substituting element can also lead to enhanced electrochemical capacity of $LiCoO_2$. For instance, silver (Ag) is a non-substituting element for $LiCoO_2$ since

* Corresponding author at: Department of Textile Engineering, Uludag University, Gorukle, Bursa 16059, Turkey. Tel.: +90 531 8311698.
** Corresponding author at: Department of Chemical and Biomolecular Engineering, North Carolina State University, Raleigh, NC 27695-7905, USA.
E-mail addresses: aykut@uludag.edu.tr (Y. Aykut), khan@eos.ncsu.edu (S.A. Khan).

0022-3697/$ - see front matter © 2013 Elsevier Ltd. All rights reserved.
http://dx.doi.org/10.1016/j.jpcs.2013.05.021

it has a higher ionic radius (~0.1 nm of tetrahedral and ~0.13 nm of octahedral) than Co^{3+} (~0.063 nm) and Li^{+} (0.059 nm), so Ag^{+} could not enter into the $LiCoO_2$ lattice [22–24]. However, the highly mobile Ag^{+} can migrate and enter into the interlayer space of $LiCoO_2$. Superior electrochemical performance, discharge and storage capacity and cycling stability of lithium-ion batteries have been overcome with Ag addition in cathode materials [24,25]. Enhanced structural stability and electrochemical properties of other cathodes such as $Li_4Ti_5O_{12}$ [26] and $LiMn_2O_4$ [27] with Ag addition have also been reported in the literature. A superior electrochemical performance with the addition of Ag to nanocrystalline $LiCoO_2$ was similarly reported by several groups [22–24].

Decreasing the particle size and increasing the specific surface area of the cathode are one of the ways to improve lithium-ion battery performance since more Li^{+} ion insertion can be obtained with the high surface area of the cathode that leads to increase activity of the cathode [3]. This implies that nanostructured $LiCoO_2$ provides superior properties for lithium-ion batteries as the cathode. The sol–gel procedure is a favorable method among other methods to produce nanostructured $LiCoO_2$ with a good homogeneity, well grain growth and good stoichiometry since all the constituent precursors can be mixed intimately [7]. $LiCoO_2$ prepared via the sol–gel procedure in the form of particles, fibers and films have been reported in the literature [6,7,13].

1D nanofibrous $LiCoO_2$ with high surface to volume ratio has been produced with combination of the sol–gel chemistry and the electrospinning technique, but the preparation of $Ag/LiCoO_2$ nanofibers is a major challenge because the atomic radii of Ag^{+} are larger than Co and Li ions that cause the loss of nanofiber uniformity during the production process and no work has been reported dealing with this until now [6,28,29]. In this study, we examine the preparation of silver/lithium cobalt oxide ($Ag/LiCoO_2$) nanofibers via sol–gel electrospinning. We report on the self-alignment of the Ag NPs in the precursor NFs, the production of $Ag/LiCoO_2$ NFs with nanoporous structure after the calcination process, and possible mechanisms leading to such structures. These $Ag/LiCoO_2$ nanofibers can be potentially used in lithium-ion batteries as efficient battery cathode.

2. Experimental methods

2.1. Chemical reagents

Lithium acetate ($LiC_2H_3O_2 \cdot 2H_2O$), cobalt acetate ($Co(CH_3COO)_2 \cdot 4H_2O$), polyvinyl alchohol (PVA, average molecular weight 127 kDa, 88% hydrolyzed) and polyvinyl pyrrolidone (PVP, molecular weight of 1300 kDa) were received from Sigma-Aldrich. $AgNO_3$ (99%) was obtained from Fisher Scientific. Deionized water (d-H_2O) was used as solvent. All chemical reagents utilized in this study were used as received without further purifications.

2.2. Synthesis of Ag NPs in aqueous PVP solution

Ag NPs, 10 wt% of PVP/water solution was prepared by magnetically stirring in a glass vial at ambient condition until a homogeneous solution was obtained. The prepared solution was left at room temperature for 2 h to allow the system to equilibrate. $AgNO_3$ was weighed and added to the PVP/water solution in a 1:2 weight ratio of $AgNO_3$/PVP, then magnetically stirred at an ambient condition. UV–vis absorption spectrum of the solution was collected every 15 min during magnetic stirring; these are reported in the next section and shown in Fig. 2. The role of PVP is to reduce Ag^{+} ions into Ag NPs and prevent potential Ag NPs aggregation. The produced Ag NPs coordinates with the O or N groups of PVP molecules, and are then covered with PVP chains that produce a layer on the particle surface to prevent potential growth and agglomeration of Ag NPs [30]. The growths of the Ag NPs are gathered by magnetically stirring. We used PVP to produce Ag NPs instead using PVA (even though we use PVA in our LiAc/$Co(Ac)_2$/PVA precursor ES solution) since the reducibility of Ag NPs by PVP is better than PVA [31].

2.3. Sol–gel electrospinning of Ag/Li(Ac)/$Co(Ac)_2$/PVA/PVP composite precursor NFs and their calcination process

A schematic illustration of the sol–gel electrospinning of $Ag/LiCoO_2$ NFs is shown in Fig. 1. A typical procedure for the preparation of electrospinning solution, 8 wt% of PVA/water solution was prepared by magnetically stirring the solution in a glass vial at 60 °C until a homogeneous solution was obtained. Then, a 1:1 wt. ratio of Li(Ac) and $Co(Ac)_2$ were weighed and added to the PVA/water solution prepared previously to obtain a 1:1 wt. ratio of (LiAc/$Co(Ac)_2$):PVA. All mixtures were magnetically stirred at 60 °C for 24 h to obtain an appropriate viscous electrospinning solution. Subsequently, the Ag/PVP/water solution was added to LiAc/$Co(Ac)_2$/PVA/water solution and magnetically stirred at ambient condition for 5 min. Three different samples were prepared at 1, 2, and 3 ml of Ag/PVP/water solutions in 10 ml LiAc/$Co(Ac)_2$/PVA/water solutions.

1 ml of the electrospinning stock solution was placed in a plastic syringe containing a stainless steel needle (0.508 mm ID). The syringe was attached to a flow control pump (0.5 ml/h). The tip of the needle faced the grounded metal plate which was covered with aluminum foil. The tip of the needle was 15 cm from the collector. A power source (Gamma High Voltage Research D-ES 30PN/M692) was connected to the needle and 15 kV voltage was applied causing a high electric field between the needle and the grounded collector. The electrostatic forces cause the formation of a polymer jet coming from the syringe tip to grounded collector. The polymer jet is elongated during its journey forming fine fibers.

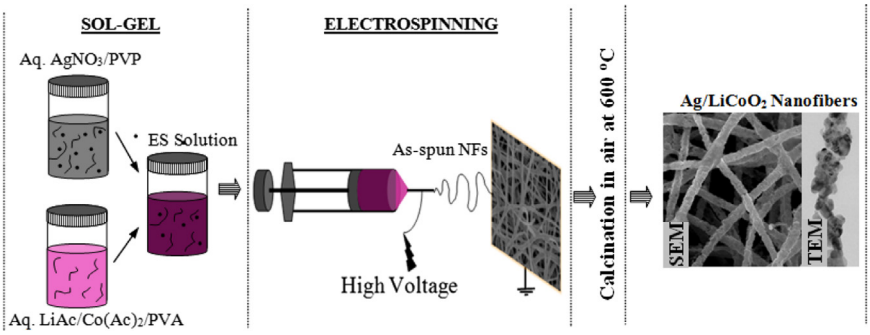

Fig. 1. Schematic illustration of the sol–gel electrospinning of $Ag/LiCoO_2$ nanofibers.

A rapid solvent evaporation occurs in this process and solidified nanofibers are collected on the grounded plate in the form of a random 3D web.

As-spun Li(Ac)/$Co(Ac)_2$/PVA and Ag/Li(Ac)/$Co(Ac)_2$/PVA/PVP NFs were calcinated in a Lindberg one-zone furnace with a quartz tube inner diameter of 45 mm (Model 58114). The calcination processes were performed in air atmosphere and air temperature was increased to 600 °C at a heating rate of 5 °C/min and maintained at that temperature for 2 h to allow proper oxidation of nanofibers and the removal of the combustion gases and other organic residues.

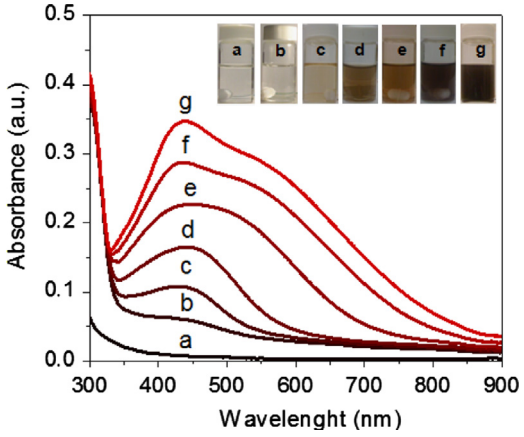

Fig. 2. UV–vis spectra of as-synthesized silver nanoparticles in PVP/water solution: all the constituents are added in the solution and the spectra are collected after (a) 0, (b) 15, (c) 30, and (d) 60 min, and (e) 2, (f) 3, and (g) 4 h magnetically stirring.

2.4. Analytical characterization of the as-synthesized Ag NPs, and as-spun Li(Ac)/$Co(Ac)_2$/PVA and Ag/Li(Ac)/$Co(Ac)_2$/PVA/PVP NFs, and calcined $LiCoO_2$ and Ag/$LiCoO_2$ NFs

UV–vis absorption spectra of Ag NPs synthesized in aqueous PVP solution were performed with a Jasco V-550 UV–vis Spectrophotometer. The spectra were collected in the wavelength range between 300 and 900 nm. PMMA cuvettes were used and disposed of after each measurement. The morphology of Li(Ac)/$Co(Ac)_2$/PVA and Ag/Li(Ac)/$Co(Ac)_2$/PVA/PVP precursor NFs and their calcinated counterparts of $LiCoO_2$ and Ag/$LiCoO_2$ ceramic NFs was screened with a field emission scanning electron microscope (FEI/Philips XL30 SEM-FEG) using an acceleration voltage of 5 kV. All samples were coated with gold at a thickness of approximately 100 Å by using a DentonVacuum Desk IV sputter coater. To screen Ag NPs in as-spun NFs, and observe the crystallized calcined nanofibers, high-magnification transmission electron microscopy (TEM) (Hitachi HF-2000) was used. For TEM, the precursor NFs were directly electrospun on the carbon coated Cu grid, and the calcinated NFs were broken apart and suspended in ethanol and placed on the Cu grid. Samples were dried in a fume hood for 24 h before the imaging. The weight loss of the precursor Li(Ac)/$Co(Ac)_2$/PVA and Ag/Li(Ac)/$Co(Ac)_2$/PVA/PVP NFs was established in air atmosphere with a thermogravimetric analyzer (TA-Instruments TGA-Q500) heating from 25 to 600 °C (heating rate of 10 °C min^{-1}). The crystalline microstructural and phase analyses of as-spun Ag/Li(Ac)/$Co(Ac)_2$/PVA/PVP and calcined $LiCoO_2$ and Ag/$LiCoO_2$ NFs were carried out with a Rigaku SmartLab® wide angle X-ray diffractometer customized auto-mount with a Cu Kα radiation source ($\lambda = 1.54$ Å) and collected the patterns in the degree range from 10° to 80° with a speed of 5°/min. The XPS spectra of the calcined Ag/$LiCoO_2$ NFs were collected on a Kratos Analytical Axis Ultra XPS system and the collected spectra was analyzed by using the CasaXPS software.

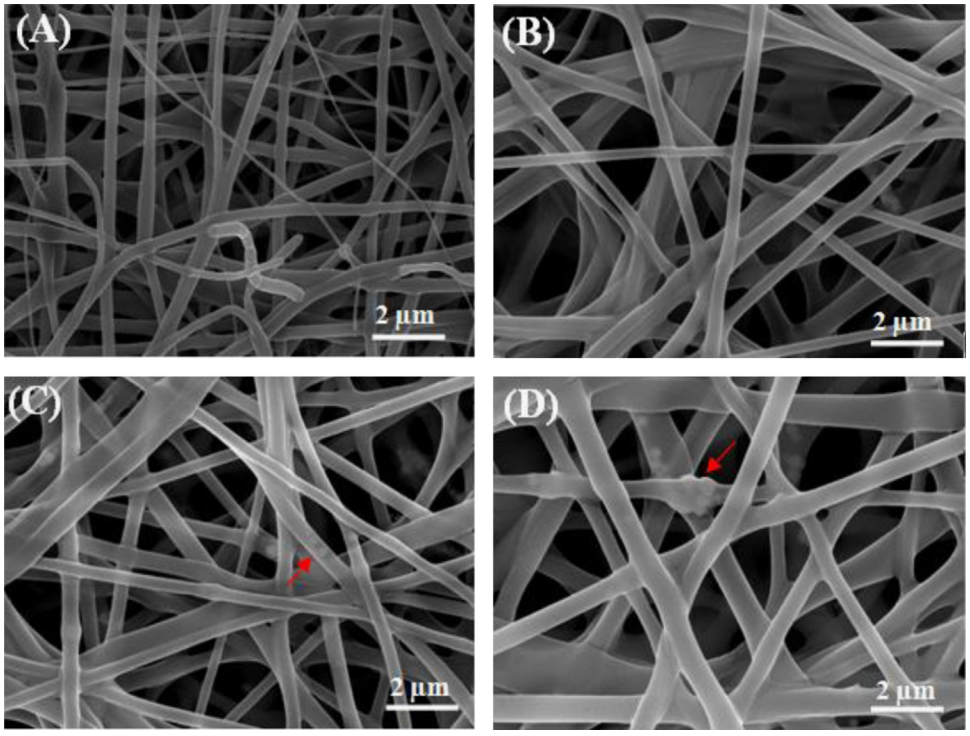

Fig. 3. SEM images of as-spun (A) Li(Ac)/$Co(Ac)_2$/PVA NFs, and Ag/Li(Ac)/$Co(Ac)_2$/PVA/PVP NFs with different Ag contents: (B) 1 wt% Ag, (C) 2 wt% Ag, and (D) 3 wt% Ag in ES solution. (For interpretation of the references to color in this figure, the reader is referred to the web version of this article.)

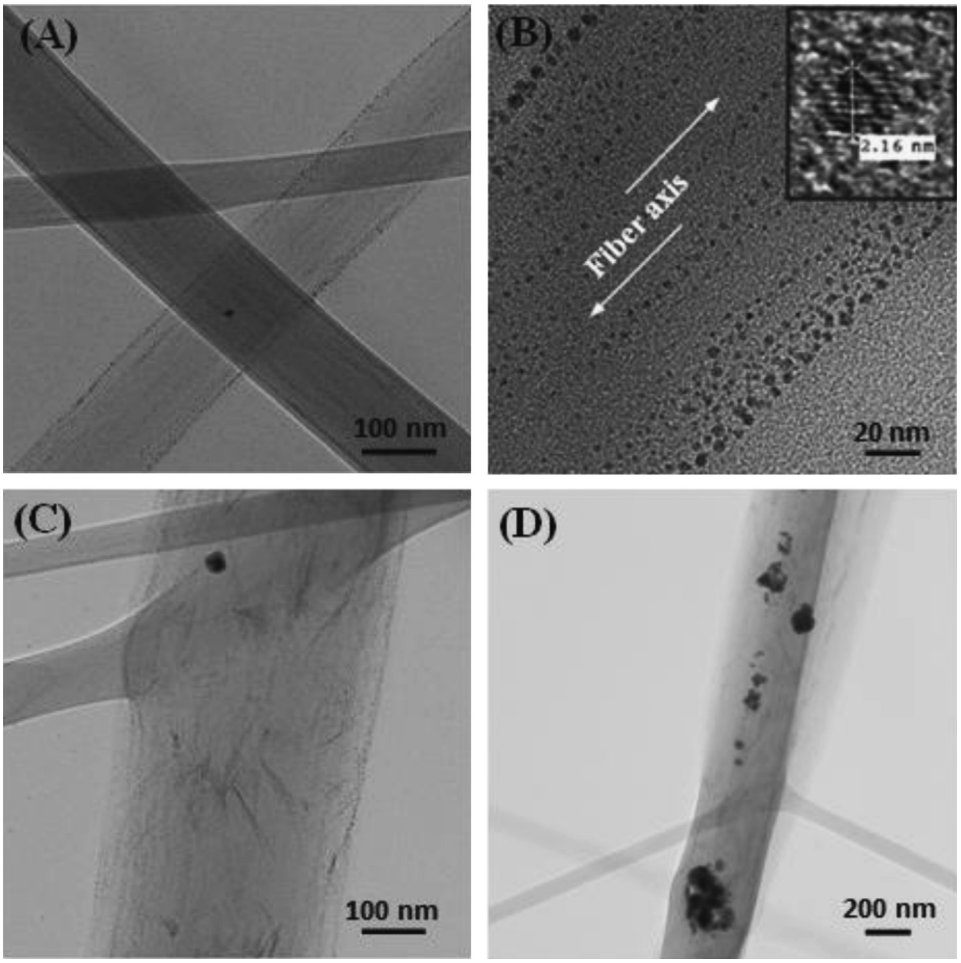

Fig. 4. TEM images of as-spun Ag/Li(Ac)/$Co(Ac)_2$/PVA/PVP NFs: (A and B) Ag nanoparticles are almost self-aligned along the nanofiber axis, and (C and D) Ag NPs agglomeration is obvious in the fibers.

3. Results and discussion

UV–vis absorption spectra of the as-synthesized Ag NPs in aqueous PVP/$AgNO_3$ solutions were monitored at the wavelength range between 300 and 900 nm, and are reported in Fig. 2. PVP chains act as a reducing agent and reduce Ag^+ ions to metal Ag and produce Ag NPs in the solution, the size of which increases with magnetically stirring. PVP also behaves as a protecting agent in the solution and inhibits the agglomeration of the particles. It is reported that Ag NPs with the diameter ranging between 2 and 50 nm absorb in the wavelength range of 400–450 nm [19,20]. A similar trend is observed in our study, and as-synthesized Ag NPs in Ag–PVP system exhibit a plasmon resonance peak at UV–vis absorption spectra in the wavelength range 300–900 nm (Fig. 2). The absorption intensity increases substantially with increasing reaction time, a so-called reduction time that leads to an increase in Ag NPs size in the solution, and absorption spectra gets broader due to increasing Ag NPs size distribution. As seen from the spectra, no absorption is observed for samples that were magnetically stirred until 15 min. Note that the color of the solution changes from transparent to a darker color when the stirring time is prolonged and this is indicative of Ag NPs generation and growth (Fig. 2). The phenomenon to produce Ag NPs in an aqueous polymer solution is explained in the experimental section and has been reported by several groups [30–32].

In order to obtain smooth nanofibers without any apparent defects in the structure, a series of electrospinning solutions were prepared and electrospun by changing the solution and process parameters. SEM images of as-spun Li(Ac)/$Co(Ac)_2$/PVA and Ag/Li(Ac)/$Co(Ac)_2$/PVA/PVP NFs are presented in Fig. 3 shows morphological changes with the addition of Ag NPs in the precursor nanofibers. All webs appear to exhibit a random fiber orientation. Li(Ac)/$Co(Ac)_2$/PVA NFs exhibit a smooth surface morphology (Fig. 3(A)) but the nanofiber surfaces get rougher with the addition of Ag NPs and Ag NPs are visible in the nanofibers, representative samples of which are highlighted with red arrows in Fig. 3(C) and

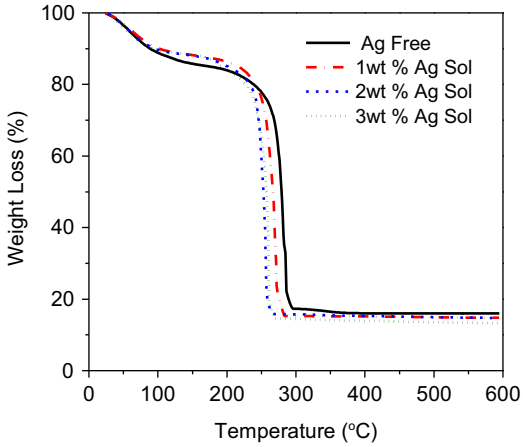

Fig. 5. TGA thermograms of as-spun Ag/Li(Ac)/$Co(Ac)_2$/PVA/PVP NFs with different Ag contents.

(D). The diameters of the fibers are in the range from 100 nm to 2 μm, and the fiber diameters obviously increase with the increasing amount of Ag NPs in the electrospinning solution.

TEM observations of as-spun precursor Ag/Li(Ac)/$Co(Ac)_2$/PVA/PVP NFs were also conducted to demonstrate Ag NPs in the fibers (Fig. 4). As seen from the images, the Ag NPs in the as-spun Ag/Li(Ac)/$Co(Ac)_2$/PVA/PVP NFs are well distributed and the particles are almost self-aligned along the nanofiber axis (Fig. 4(A) and (B)). This is caused by the electrical field that is created in the ES setup between the metal needle and the grounded collector metal plate during the electrospinning process. Some Ag NPs appear to be clustered in Ag/Li(Ac)/$Co(Ac)_2$/PVA/PVP precursor NFs (Fig. 4 (C) and (D)), but this is not very common in the samples studied. High magnification of a single Ag NP in an as-spun precursor NF is shown inset of Fig. 4(B). Crystal lattice fringes of Ag the NP can be seen in this image.

Thermogravimetric analysis of the precursors Li(Ac)/$Co(Ac)_2$/PVA and Ag/Li(Ac)/$Co(Ac)_2$/PVA/PVP NFs were performed to

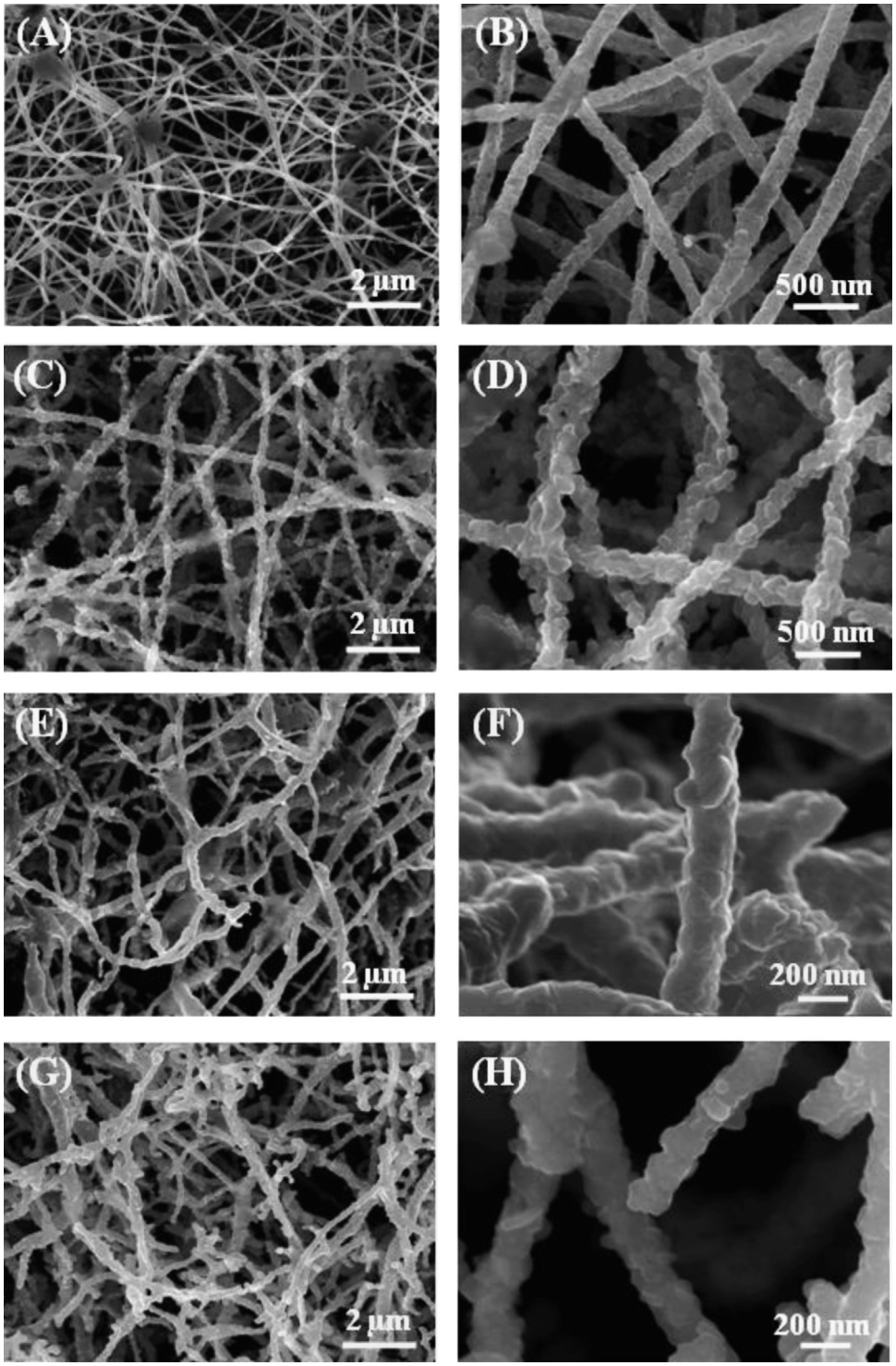

Fig. 6. SEM images of (A and B) $LiCoO_2$ NFs, and (C and D) Ag/$LiCoO_2$ NFs with 1 wt% Ag, (E and F) Ag/$LiCoO_2$ NFs with 2 wt% Ag, and (G and H) Ag/$LiCoO_2$ NFs with 3 wt% Ag contents.

distinguish the weight loss and oxidation of the fibers during the calcination process (Fig. 5) The weight loss in the temperature range 25–100 °C is attributed to the weight loss of water molecules that are held by the nanofibers. Organic components belonging to PVA, PVP, and CH_3COO group of lithium acetate and cobalt acetate decomposed up until ~285 °C, after which, no further weight loss is observed. Clearly, a sharp weight loss occurs between ~210 and ~297 °C. The addition of Ag NPs shifts the decomposed temperature range to a lower range. This may be attributed to the less thermally stable property of PVA than PVP and PVA content increases in the final precursor NFs when we added NPs that were in aqueous PVP solution [33]. The amount of residues of the fibers after TGA measurement decreases slightly with increasing Ag content in the precursor Ag/Li(Ac)/$Co(Ac)_2$/PVA/PVP NFs because the amount of the organic constituent increases in the precursor NFs. After thermal decomposition, the residuals remaining in the Ag/$LiCoO_2$ nanofibers are 15.9%, 14.8%, 14.7%, and 13.3% respectively for 0, 1, 2, and 3 wt% of Ag/PVP in Ag/Li(Ac)/$Co(Ac)_2$/PVA/PVP precursor NFs.

SEM images of calcined $LiCoO_2$ (Fig. 6(A)) and Ag/$LiCoO_2$ (Fig. 6 (C)–(H)) NFs are shown in Fig. 6. After calcination, the fibers shrink and the average fiber diameter decreases significantly as a result of mass loss. With increasing temperature, most of the Ag NPs are gradually oxidized and above 500 °C, almost all of the oxygen atoms diffuse and escape from the AgO particles and only the Ag phase remains in the NFs [34]. The atomic radii of Ag are significantly higher than that of Co and Li, which prevent diffusion and insertion of Ag atoms in $LiCoO_2$ NFs. The surfaces of Ag-doped $LiCoO_2$ nanofibers are extremely rough (Fig. 6(C)–(H)) because many of the Ag particles formed on the surface detaches from the fibers. These particles cannot bond strongly to the fibers, and nanoporous structures in the fibers are observed, and some fiber breakage is seen. This can be seen in detail from the TEM images of the samples (Fig. 7). As seen, $LiCoO_2$ NFs are composed of $LiCoO_2$ nanoparticles. Voids in Ag/$LiCoO_2$ fibers are evident (Fig. 7(B)) because some of the Ag NPs disengages from the fibers and the surface of the fiber is not as smooth as un-doped $LiCoO_2$ nanofibers (Fig. 7(A)). The measured crystal lattice fringe d-spacing of $LiCoO_2$ nanofibers is ~0.241 nm (Fig. 7(C)).

XRD patterns of as-spun Ag/Li(Ac)/$Co(Ac)_2$/PVA/PVP, and calcinated $LiCoO_2$ and Ag/$LiCoO_2$ NFs were examined to investigate the crystalline structures of the fibers and Ag NPs in the nanofibers before and after calcination (Fig. 8). As seen from the XRD pattern of Ag/Li(Ac)/$Co(Ac)_2$/PVA/PVP NFs in Fig. 8(a), the peak at $2\theta=20^\circ$ represents the semicrystalline PVA in the NF precursor and corresponds to a (101) crystal plane [8]. The peaks coming from Ag NPs are centered at $2\theta\approx38.1^\circ$ and 44.25° and correspond to (111) and (200) crystal planes of the face-centered cubic (fcc) of Ag [31].

As seen in the X-ray spectral patterns in Fig. 8(b), electrospun crystalline $LiCoO_2$ NFs calcined at 600 °C give reflection peaks centered at $2\theta\approx18.9^\circ$, 37.4°, 38.9°, 45.2°, 49.3°, 59.6°, 65.6°, 66.3° and 69.6° that correspond to the (003), (101), (012), (104), (105), (107), (108), (110) and (113) crystal planes [6,13]. The peak located at $2\theta\approx31.7^\circ$ corresponds to the (220) crystal plane and comes from the small amount Co_3O_4 crystals formed. These crystals are not observed with Ag/$LiCoO_2$ nanofibers [35–37]. The intensity of the Ag peaks is slightly higher for the calcined nanofiber compared to the uncalcined Ag/Li(Ac)/$Co(Ac)_2$/PVA/PVP NF because crystallinity of calcined Ag NP after calcinations increases. But there are still uncrystallized Ag^+ in the precursor nanofiber sample which converts to AgO upon calcinations. The diffraction pattern of Ag/$LiCoO_2$ NFs is shown in Fig. 8(c) in which the peaks from silver crystals are located at $2\theta\approx38.1^\circ$, 44.3°, 64.5°, and 77.3° and correspond to (111), (200), 220 and 311 cubic crystal planes of fcc crystalline Ag; the $LiCoO_2$ peaks are observed at $2\theta\approx19.5^\circ$, 37.3°, 39.1°, 45.2°, 49.4°, 60°, 64.4°, 66.1° and 69.7° and correspond to the (003), (101), (012), (104), (105), (107), (108), (110) and (113) crystal planes. [22,38,39] No shift in the diffraction angles of $LiCoO_2$ peaks is observed with Ag addition, thereby indicating that the highly mobile Ag^+ (~0.1 nm) migrates and enters into interlayer space of

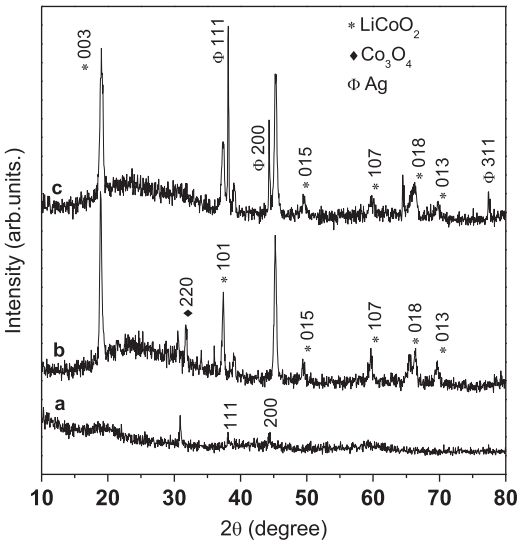

Fig. 8. X-ray diffraction of (a) as-spun Ag/Li (Ac)$Co(Ac)_2$/PVA/PVP, and calcined, (b) $LiCoO_2$, and (c) Ag/$LiCoO_2$ nanofibers.

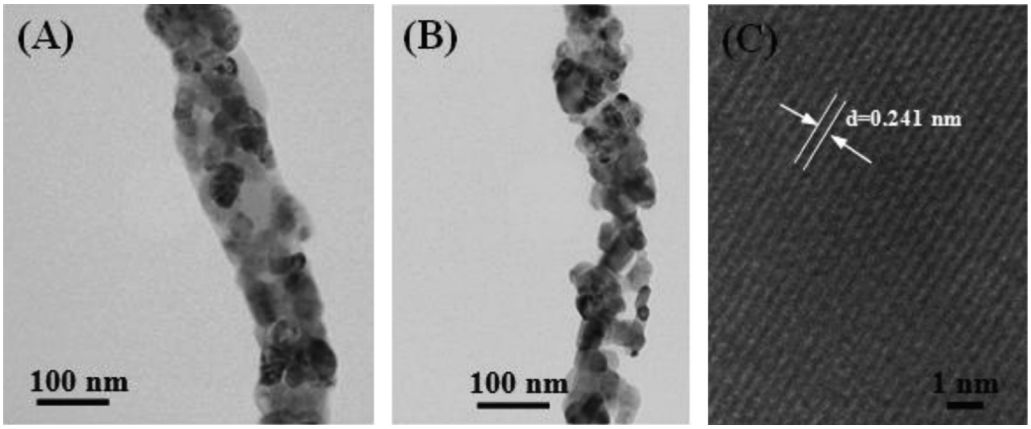

Fig. 7. TEM images of calcined (A) $LiCoO_2$ NF, (B) Ag/$LiCoO_2$ NF, and (C) lattice spacing of (101) plane of $LiCoO_2$ NFs.

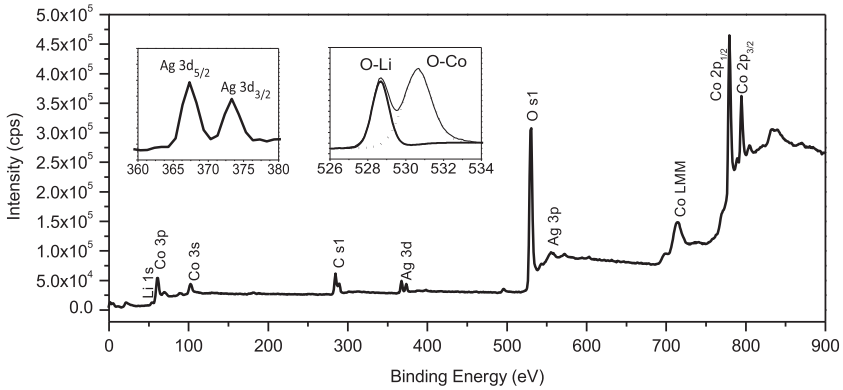

Fig. 9. XPS spectra of calcined Ag/$LiCoO_2$ nanofibers.

$LiCoO_2$ during the calcination process but does not substitute either the Li (0.059 nm), or Co (~0.063 nm) atoms. So, some Ag^+ diffuse to the surface and leave from the fibers, whereas some Ag^+ get reduced to AgO and forms Ag NP in $LiCoO_2$ nanofibers. During the calcination process, the Ag nanoparticles in the precursor nanofibers are first oxidized and then reduced to metallic Ag NPs after the temperature reach and pass 500 °C [34]. In the Ag/LiCoO2 sample, only metallic Ag phase is evident. Based on Bragg's law, as-measured and calculated from the XRD results, the lattice constants of the fcc silver crystals in the un-doped and Ag doped $LiCoO_2$ are similar (~2.41 Å) and correspond to the (101) plane of $LiCoO_2$ consistent with the lattice constant found in the literature [40].

X-ray photoelectron spectroscopy (XPS) analysis of Ag/$LiCoO_2$ was also conducted and reported in Fig. 9 for Ag NPs in $LiCoO_2$ nanofibers. Spectral peaks for Li, Co3p, Co3s, Cs1, Ag $3d_{5/2}$, Ag $3d_{3/2}$, Os1, CoLMM, Co2p, Co2p, and CoLMMc are assigned and centered at 57.3, 61.3, 104.3, 284.3, 367.3, 373.3, 530, 716.3, 779, 794, and 840 sequentially. Two spectral peaks were detected for Ag NPs with binding energies (BE) of 367.3 eV and 373.3 eV in Ag/$LiCoO_2$ NFs and can be assigned to the spectra of Ag $3d_{5/2}$ and Ag $3d_{3/2}$ respectively that is indicative of the formation and existence of Ag NPs in the fibers [38]. Kim et al. performed XPS analysis of $AgNO_3$ and detected a single peak of the spectra of Ag $3d_{5/2}$ at 370.3[41]. Co2p core peaks is detected as two parts, of $Co2p_{3/2}$ and $Co2p_{1/2}$ (at 779 and 794 eV binding energies) as a result of spin–orbital coupling; each part consists of a main line and a satellite peak (at 779 and 794 eV binding energies) suggestive of the existence of Co^{3+} and Co^{4+} ions in $LiCoO_2$ nanofibers [42]. The satellites peaks have higher binding energy than the main peaks. The Li 1s core peak appears at 57.3 eV corresponding to lithium atoms in a tetrahedral environment of oxygen atoms in $LiCoO_2$ [43]. The peak centered at 530 eV is attributed to O^{2-} anions in the crystal structure, and the peak at 284.3 eV is assigned to Cs1 that can be attributed to the organic contaminants that came from the environment while processing and characterizing the sample [42]. To further determine the binding of Li and Co with O, XPS measurements were carried out and demonstrated at inset figure of Fig. 9. As can be seen, the binding of Co with O is a little higher than the binding of Li with O. XRD and XPS results are indicative of the successful preparation of electrospun Ag/$LiCoO_2$ nanofibers in this study.

4. Conclusions

In this study, we report on a facile preparation of Ag-doped $LiCoO_2$ NFs via a sol–gel electrospinning technique. Ag NPs were fabricated in aqueous PVP solution, and a proper amount of this mixture was added into the LiAc/$(CoAc)_2$/PVA electrospinning solution to produce Ag/LiAc/$(CoAc)_2$/PVA/PVP precursor NFs. Well distributed Ag NPs in the precursor Ag/LiAc/$(CoAc)_2$/PVA/PVP NFs were produced and these NFs were calcined at 600 °C in air atmosphere for 3 h. Self-alignment of Ag NPs in the precursor NFs was observed which may have attributed to the behavior of Ag NPs in the electrical filed that is created in the ES setup. Ag/$LiCoO_2$ NFs with nanoporous structure were obtained after the calcination process. The porous structure was possibly caused by the Ag NPs leaving the fibers during the calcination process since the atomic radius of Ag ions is bigger than Li and Co ions to substitute them in the $LiCoO_2$ NFs. The Ag phases thus exist only at the interlayers of $LiCoO_2$ crystals in the NFs. The prepared Ag-doped $LiCoO_2$ NFs can be used as the cathode material in Li-ion batteries.

Acknowledgment

The authors acknowledge the funding support from the Non-wovens Cooperative Research Center, NCRC at North Carolina State University and the Ministry of National Education of the Republic of Turkey. YA thanks Dr. Dale Bachelor of the Analytical Instrumentation Facility, NCSU, and Dr. Mark D. Walters of the Shared Materials Instrumentation Facility at Duke University for their assistance in sample characterization.

References

[1] I. Nakai, K. Takahashi, Y. Shiraishi, T. Nakagome, F. Nishikawa, J. Solid State Chem. 140 (1998) 145.
[2] E.M. Sorensen, S.J. Barry, H.K. Jung, J.R. Rondinelli, J.T. Vaughey, K.R. Poeppelmeier, Chem. Mater. 18 (2006) 482.
[3] F.F.C. Bazito, R.M.J. Torresi, J. Braz, J. Braz. Chem. Soc. 17 (2006) 627.
[4] H. Arai, S. Okada, Y. Sakurai, J.I. Yamaki, Solid State Ionics 106 (1998) 45.
[5] J. Cho, B. Park, Electrochem. Solid State Lett. 3 (2000) 355.
[6] Y. Gu, D. Chen, X. Jiao, J. Phys. Chem. B 109 (2005) 17901.
[7] W.S. Yoon, K.B. Kim, J. Power Sources 81 (1999) 517.
[8] C. Shao, N. Yu, Y. Liu, R.J. Mu, Phys. Chem. Solids 67 (2006) 1423.
[9] T. Kawamura, M. Makidera, S. Okada, K. Koga, N. Miura, J. Yamaki, J. Power Sources 146 (2005) 27.
[10] J.C. Dupin, D. Gonbeau, H. Benqlilou-Moudden, P. Vinatier, A. Levasseur, Thin Solid Films 384 (2001) 23.
[11] E. Grigorova, T.S. Mandzhukova, M. Khristov, M. Yoncheva, R. Stoyanova, E. Zhecheva, J. Mater. Sci. 46 (2001) 7106.
[12] D. Ensling, A. Thissen, S. Laubach, P.C. Schmidt, W. Jaegermann, Phys. Rev. B 82 (2010) 19531.
[13] X. Qian, X. Cheng, Z. Wang, X. Huang, R. Guo, D. Mao, C. Chang, W. Song, Nanotechnology 20 (2009) 115608.
[14] S.M. Lala, L.A. Montoro, J.M. Rosolen, J. Power Sources 124 (2003) 118.
[15] S.M. Lala, L.A. Montoro, E.D. Donato, J.M. Rosolen, J. Power Sources 114 (2003) 127.
[16] R. Alcantara, P. Lavela, J.L. Tirado, R. Stoyano, E. Zhecheva, J. Solid State Chem. 134 (1997) 265.
[17] S. Waki, K. Dokko, T. Itoh, M. Nishizawa, T. Abe, I. Uchida, J. Solid State Electrochem. 4 (2000) 205.
[18] R. Stoyanova, E. Zhecheva, L. Zarkova, Solid State Ionics 73 (1994) 233.

[19] M. Mladenov, R. Stoyanova, E. Zhecheva, S. Vassilev, Electrochem. Commun. 3 (2001) 410.
[20] S. Madhavi, G.V. Subba Rao, B.V.R. Chowdari, S.F.Y. Li, Electrochim. Acta 48 (2002) 219.
[21] S. Gopukumar, Y. Jeong, K.B. Kim, Solid State Ionics 159 (2003) 223.
[22] S. Huang, Z. Wen, X. Yang, Z. Gu, X. Xu, J. Power Sources 148 (2005) 72.
[23] P. Ghosh, S. Mahanty, R.N. Basu, Mater. Chem. Phys. 110 (2008) 406.
[24] H.S. Kim, W.I. Cho, B.W. Cho, J.B. Ju, J. Power Sources 107 (2002) 133.
[25] S. Huang, Z. Wen, J. Zhang, X. Yang, Electrochim. Acta 52 (2007) 3704.
[26] S. Huang, Z. Wen, X. Zhu, Z. Gu, Electrochem. Commun. 6 (2004) 1093.
[27] J.T. Son, K.S. Park, H.G. Kim, H.T. Chung, J. Power Sources 126 (2004) 182.
[28] L.J. Chen, J.D. Liao, Y.J. Chuang, K.C. Hsu, Y.F. Chiang, J. Appl. Polym. Sci. 121 (2011) 154.
[29] H.W. Lu, W. Zeng, Y.S. Li, Z.W. Fu, Electrochem. Solid State Lett. 11 (2008) 140.
[30] H. Wang, X. Qiao, J. Chen, X. Wang, S. Ding, Mater. Chem. Phys. 94 (2005) 449.
[31] G. Dong, X. Xiao, X. Liu, B. Qian, Z. Ma, S. Ye, D. Chen, J. Qiu, J. Nanopart. Res. 12 (2010) 1319.
[32] C.D. Saquing, J.L. Manasco, S.A. Khan, Small 5 (2009) 944.
[33] J. Qiao, J. Fu, R. Lin, J. Ma, J. Liu, Polymer 51 (2010) 4850.
[34] X.Y. Gao, S.Y. Wang, J. Li, Y.X. Zheng, R.J. Zhang, P. Zhou, Y.M. Yang, L.Y. Chen, Thin Solid Films 455–456 (2004) 438.
[35] G. Wang, J. Liu, S. Tang, H. Li, D.J. Cao, Solid State Electrochem. 15 (2011) 2587.
[36] F. Gu, C. Li, Y. Hu, L.J. Zhang, J. Cryst. Growth 304 (2007) 369.
[37] N.A.M. Barakat, M.S. Khil, F.A. Sheikh, H.Y. Kim, J. Phys. Chem. C 112 (2008) 12225.
[38] Y. Gao, P. Jiang, D.F. Liu, H.J. Yuan, X.Q. Yan, Z.P. Zhou, J.X. Wang, L. Song, L.F. Liu, W.Y. Zhou, G. Wang, C.Y. Wang, S.S. Xie, J.M. Zhang, D.Y.J. Shen, Phys. Chem. B 108 (2004) 12877.
[39] J. Huang, Q. Li, D. Sun, Y. Lu, Y. Su, X. Yang, H. Wang, Y. Wang, W. Shao, N. He, J. Hong, C. Chen, Nanotechnology 18 (2007) 105104.
[40] S. Jeong, S. Park, J. Cho, Adv. Energy Mater. 1 (2011) 368.
[41] Y.W. Kim, D.K. Lee, K.J. Lee, B.R. Min, J.H. Kim, J. Polym. Sci. Part B: Polym. Phys 45 (2007) 1283.
[42] L. Daheron, R. Dedryvere, H. Martinez, M. Menetrier, C. Denage, C. Delmas, D. Gonbeau, Chem. Mater. 20 (2008) 583.
[43] R. Alcantra, G.F. Ortiz, P. Lavela, J.L. Tirado, W. Jaegermann, A. Thisen, J. Electroanal. Chem. 584 (2005) 147.